In Vivo Molecular Photoacoustic Tomography of Melanomas Targeted by Bioconjugated Gold Nanocages

Chulhong Kim,[†,§] Eun Chul Cho,[†,§] Jingyi Chen,[†] Kwang Hyun Song,[†] Leslie Au,[†] Christopher Favazza,[†] Qiang Zhang,[†] Claire M. Cobley,[†] Feng Gao,[‡] Younan Xia,[†,*] and Lihong V. Wang[†,*]

[†]Department of Biomedical Engineering, Washington University in St. Louis, Campus box 1097, One Brookings Drive, St. Louis, Missouri 63130 and [‡]Division of Biostatistics, Washington University School of Medicine, Campus box 8067, 660 South Euclid Avenue, St. Louis, Missouri 63110. [§]These authors contributed equally to this work.

ABSTRACT Early diagnosis, accurate staging, and image-guided resection of melanomas remain crucial clinical objectives for improving patient survival and treatment outcomes. Conventional techniques cannot meet this demand because of the low sensitivity, low specificity, poor spatial resolution, shallow penetration, and/or ionizing radiation. Here we overcome such limitations by combining high-resolution photoacoustic tomography (PAT) with extraordinarily optical absorbing gold nanocages (AuNCs). When bioconjugated with [Nle^4,D-Phe^7]-α-melanocyte-stimulating hormone, the AuNCs can serve as a novel contrast agent for *in vivo* molecular PAT of melanomas with both exquisite sensitivity and high specificity. The bioconjugated AuNCs enhanced contrast ~300% more than the control, PEGylated AuNCs. The *in vivo* PAT quantification of the amount of AuNCs accumulated in melanomas was further validated with inductively coupled plasma mass spectrometry (ICP-MS).

KEYWORDS: photoacoustic tomography · gold nanocages · melanoma · bioconjugation · molecular imaging

The 10 year survival rate of early stage cutaneous melanoma patients is very high (~99%), but the rate drops to 40% after nodal metastases.[1,2] Thick melanomas (>4 mm) are typically associated with a high risk of nodal and distant metastases. Highly sensitive molecular imaging techniques including positron emission tomography (PET) and optical imaging have been developed for detecting early stage melanomas.[3−5] However, PET requires on the use of radio-labeling materials, which can cause potential hazards to patients. Moreover, it suffers from low spatial resolution and high cost due to the need of additional anatomical information from magnetic resonance imaging (MRI) and/or X-ray computed tomography (CT). Since optical imaging uses non-ionizing radiation and is cost-effective, it has received much attention in molecular imaging.[6] However, conventional optical imaging tools are often limited by either shallow penetration depth (<1 mm)[7] or poor spatial resolution.[8] Besides early detection, accurate delineation of the margins of a melanoma can significantly improve surgical removal of the primary tumor. High-frequency ultrasound has been applied preoperatively for this purpose,[9] but it cannot effectively resolve the margins of a melanoma and does not infiltrate cells. Additionally, accurate staging (describing cancer metastasis, typically with numbers I to IV) of patients after nodal metastases is important for treatment planning.[10] Again, the current technique based on sentinel lymph node biopsy is ionizing and intraoperative and thus poses postoperative complications. These limitations of the current techniques suggest a strong need for a single, highly sensitive, safe, economical, noninvasive, and high-resolution imaging technique with nonradioactive contrast agents in early diagnosis of malignant melanomas, image-guided resection of melanoma boundaries, and accurate staging of melanoma patients.

Photoacoustic tomography (PAT) is a hybrid biomedical imaging modality that offers both strong optical absorption contrast and high ultrasonic resolution (Supporting Information).[11,12] Since the spatial resolution beyond one optical transport mean free path (~1 mm) is determined by ultrasonic parameters, the maximum imaging depth and resolution of PAT are scalable when diffusive photons are available.[13−15] By using a near-infrared (NIR) light, one can greatly increase the penetration depth of PAT because the optical absorption of hemoglobin and scattering of tissues are weak in this regime. However, it remains a challenge to

*Address correspondence to lhwang@biomed.wustl.edu for photoacoustic tomography, xia@biomed.wustl.edu for gold nanocages and bioconjugation.

Received for review April 9, 2010 and accepted July 06, 2010.

Published online July 13, 2010.
10.1021/nn100736c

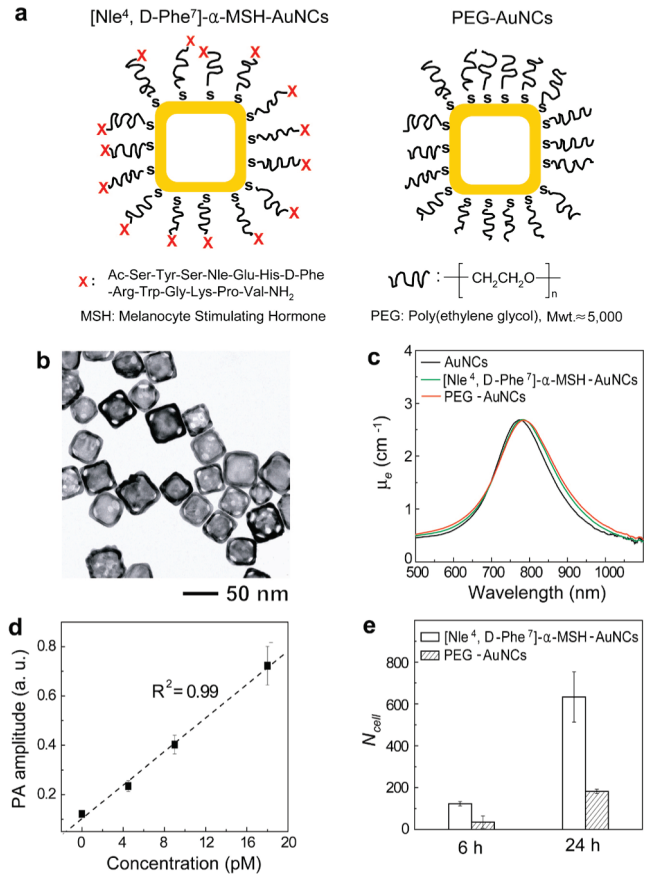

Figure 1. Schematic, characterization, photoacoustic properties, and cellular uptake of the AuNCs. (a) [Nle^4,D-Phe^7]-α-MSH-AuNCs (left) and PEG-AuNCs (right). (b) Typical transmission electron microscopy image of the AuNCs. (c) UV−vis−NIR spectra of the AuNCs (18 pM) conjugated with different chemical agents; μ_e is the extinction coefficient. (d) Plot of the PA amplitude as a function of AuNCs concentration. (e) *In vitro* uptake of [Nle^4,D-Phe^7]-α-MSH-AuNCs and PEG-AuNCs by B16 melanoma cells as determined by ICP-MS. Here N_{cell} denotes the number of AuNCs per B16 melanoma cell ($p = 0.0005$ at 6 h and $p = 0.007$ at 24 h).

assess melanomas using only morphological and functional PAT based on intrinsic contrasts such as tumor hypoxia and angiogenesis. Therefore, a tumor-specific, exogenous contrast agent is necessary for the assessment of early stage melanomas, image-guided resection, and accurate staging by PAT, with high sensitivity and specificity. Organic dyes such as IRDye-800 and indocyanine green have been used as contrast agents for PAT,[16−18] but these small molecules tend to suffer from fast clearance times and relatively small optical absorption cross sections. Recently, Au-based nanostructures[19,20] and single-walled carbon nanotubes (SWCNTs)[21] have been demonstrated as contrast agents for PAT. Despite the impressive results, there is still ongoing debate on the toxicity of SWCNTs for *in vivo* applications.[22−24] In contrast, Au-based nanostructures have been approved by FDA as drug carriers or therapeutic agents for various phase-I clinical trials (*e.g.*, http://www.cytimmune.com and http://www.nanospectra.com). AuNCs represent an excellent candidate for serving as a photoacoustic (PA) contrast agent because of its strong and tunable light absorption in the NIR region, bioinertness, easiness of bioconjugation with a tumor-specific ligand, and the enhanced permeability and retention effect.[25−27]

RESULTS

The main objective of this study is to evaluate and quantitatively compare the PA contrast enhancement on B16 melanomas provided by both active and passive targeting AuNCs. In these cases, the surface of the AuNCs was derivatized, respectively, with [Nle^4,D-Phe^7]-α-melanocyte-stimulating hormone ([Nle^4,D-Phe^7]-α-MSH-AuNCs) and poly(ethylene glycol) (PEG-AuNCs).[25,28] Figure 1a shows a schematic of the [Nle^4,D-Phe^7]-α-MSH- and PEG-AuNCs. The difference between these two AuNCs is the presence of [Nle^4,D-Phe^7]-α-MSH at the distal end of PEG chain. [Nle^4,D-Phe^7]-α-MSH has been shown to strongly bind to α-MSH receptors overexpressed on melanomas and has higher resistance to enzymatic degradation and higher specificity than the conventional α-MSH.[29,30] We focused on AuNCs with an outer edge length of 46 nm and a wall thickness of 7 nm (Figure 1b). Upon surface modification, the optical resonance peak of the AuNCs was slightly red-shifted due to minor change in refractive index on the surface (Figure 1c). The absorption cross section of the AuNCs were measured as 1.7×10^{-14} m^2, and the ratio of absorption to extinction cross sections was 0.7, confirming that the AuNCs absorb light very strongly (Supporting Information).[26] In a phantom, we could still detect PA signals from the AuNCs at a particle concentration of 4.5 pM and a signal-to-noise ratio (SNR) of 9 (Figure 1d and Supporting Information). This detection limit corresponds to $\sim 9 \times 10^{-21}$ mol of AuNCs per imaging voxel. From *in vitro* studies, the two types of AuNCs were shown to have different binding affinities toward melanomas (Figure 1e). The cellular uptake of [Nle^4,D-Phe^7]-α-MSH-AuNCs was ~3.5 times higher than that of PEG-AuNCs after 6 h (123 ± 11 *vs* 35 ± 30, $p = 0.0005$, and the unit is the number of AuNCs per B16 melanoma cell) or 24 h incubation (633 ± 121 *vs* 182 ± 10, $p = 0.007$). On the basis of the measured sensitivity limit (4.5 pM), ~5000 AuNCs per imaging voxel are required to be detected by our PAT system.

Figure 2a shows an experimental setup of the PAT system. We used macroscopic (10 MHz ultrasonic frequency) and microscopic (50 MHz ultrasonic frequency) dark-field PAT systems to image the melanoma and its surrounding microvasculatures, respectively. We used a light source at 778 nm for melanoma imaging and a light source at 570 nm for blood vessel imaging. We first acquired *in vivo* noninvasive morphological and functional PA images of mice bearing melanomas using intrinsic contrasts (melanin and hemoglobin). In Figure

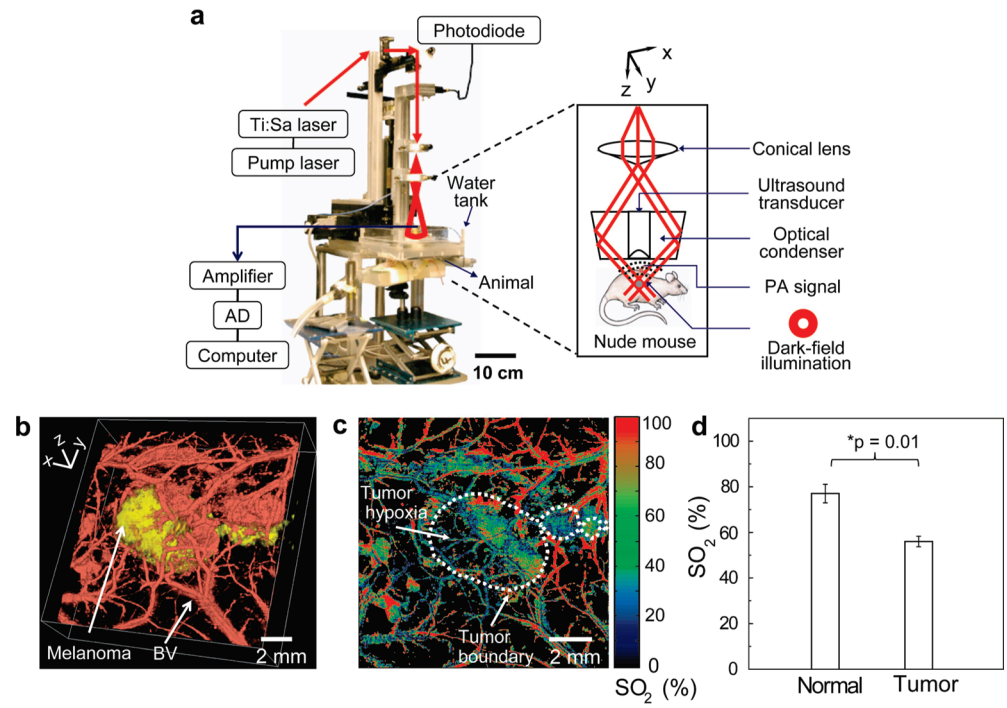

Figure 2. Experimental setup of the PA imaging system and noninvasive morphological and functional PA images of B16 melanomas *in vivo*. (a) Photograph of the PA macroscope. The schematic in the dashed box shows a dark-field, confocal configuration. (b) Volumetric morphological PA image of B16 melanoma (yellow) and its surrounding blood vessels (red). BV, blood vessels. The melanoma was imaged using the PA macroscope at 778 nm (ultrasonic frequency = 10 MHz), and the surrounding vasculatures were obtained using a PA microscope at 570 nm (ultrasonic frequency = 50 MHz). (c) PA MAP mapping of hemoglobin oxygen saturation (SO_2) of blood vessels surrounding the melanoma using two optical wavelengths of 564 and 570 nm. The white dotted line shows the tumor boundary. (d) Statistical analysis of the average SO_2 in normal mice skins and tumor hypoxic area. The average SO_2 values in normal mice skins and tumor hypoxic regions are 77 ± 7 and 56 ± 4%, respectively (p = 0.01 and n = 3 mice for each group).

2b, the tumor and tumor-feeding blood vessels are clearly seen in the volumetric structural PA images (Supporting Information movie). We also identified the tumor hypoxia by mapping the hemoglobin oxygen saturation (SO_2) of blood vessels within the melanoma at two different wavelengths, 564 and 570 nm (Figure 2c and Supporting Information Figure S1 for SO_2 mapping in a normal mouse). The average SO_2 value in tumor hypoxic regions (56 ± 4%) was less than that (77 ± 7%) in normal mice skin (p = 0.01 and n = 3 mice for each group), which is consistent with previously reported results.[16]

We then performed *in vivo* molecular PAT of melanomas for two groups of mice: one group (n = 4) with [Nle^4,D-Phe^7]-α-MSH-AuNCs and the other group (n = 4) with PEG-AuNCs. Figure 3a,e shows photographs of subcutaneous melanomas in the mice. Prior to AuNC injection, two control images were acquired for each group (Figure 3b,f) by using the 10 MHz macroscopic and 50 MHz microscopic systems to resolve melanoma and blood vessels, respectively. Then, 100 μL of either [Nle^4,D-Phe^7]-α-MSH- or PEG-AuNCs at a particle concentration of 10 nM was intravenously injected into each mouse *via* a tail vein. A series of PA images were obtained up to 6 h postinjection. The differential images of the melanomas before and after injection (*i.e.*, images after injection minus images before injection) were overlaid on the images of blood vessels. As shown in Figure 3b−d,f−h, the melanomas clearly show difference in PA signal enhancement for the two types of AuNCs (Supporting Information Figure S2 for raw images). The average PA signal (golden color) within the melanoma at 6 h postinjection of [Nle^4,D-Phe^7]-α-MSH-AuNCs increased by up to 36% (Figure 3d), whereas the increase only reached 14% for PEG-AuNCs (Figure 3h). The observed PA signal enhancement for PEG-AuNCs correlates well with previous results based on the PEGylated gold nanoshells.[20]

We plotted the PA signal enhancement in the melanomas as a function of postinjection time (Figure 4a). The trend of the PA signal enhancement over time from the bioconjugated AuNCs was significantly different (p = 0.0003) from that of the control PEG-AuNCs. The PA signals with [Nle^4,D-Phe^7]-α-MSH-AuNCs increased steeply in the beginning and then slowly up to 6 h postinjection. In contrast, those with PEG-AuNCs showed a gradual increase until 5 h postinjection and then a plateau. At 6 h postinjection, the enhancement with [Nle^4,D-Phe^7]-α-MSH-AuNCs (38 ± 6%) was on average 300% greater than that with PEG-AuNCs (13 ± 2%) (p < 0.0001). This result demonstrates that the

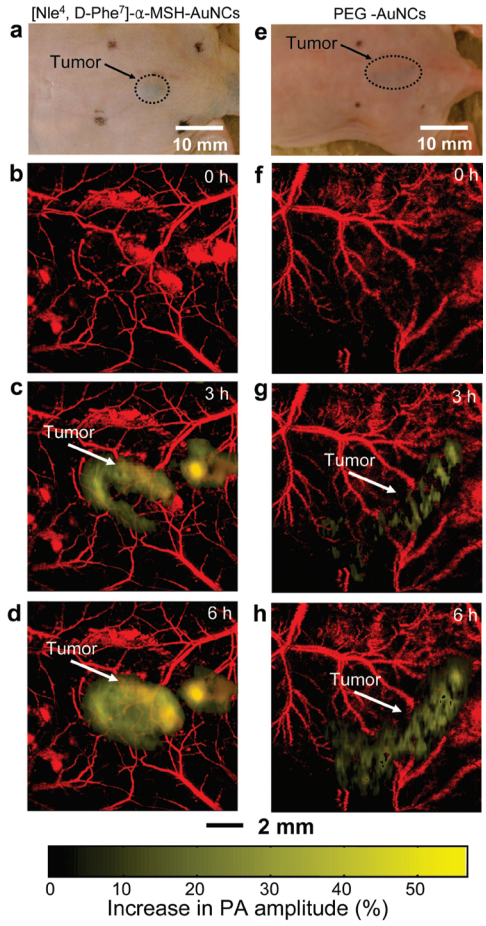

Figure 3. ***In vivo*** **noninvasive PA time-course coronal MAP images of B16 melanomas using [Nle^4,D-Phe^7]-α-MSH- and PEG-AuNCs. (a,e) Photographs of nude mice transplanted with B16 melanomas before injection of (a) [Nle^4,D-Phe^7]-α-MSH- and (e) PEG-AuNCs. Time-course PA images of the B16 melanomas after intravenous injection with 100 μL of 10 nM (b−d) [Nle^4,D-Phe^7]-α-MSH- and (f−h) PEG-AuNCs through the tail vein. The background vasculature images were obtained using the PA microscope at 570 nm (ultrasonic frequency = 50 MHz), and the melanoma images were obtained using the PA macroscope at 778 nm (ultrasonic frequency = 10 MHz). Color schemes: red for blood vessels and yellow for the increase in PA amplitude.**

[Nle^4,D-Phe^7]-α-MSH-AuNCs had a better chance to be accumulated in the tumors than the PEG-AuNCs. To verify this, we quantified the number of AuNCs accumulated in the excised tumors after PA imaging (6 h postinjection) using ICP-MS (Figure 4b). The average number of [Nle^4,D-Phe^7]-α-MSH-AuNCs per tumor mass ((3.6 ± 1.0) × 10^8 AuNCs/g) was 360% (p = 0.02) higher than that of PEG-AuNCs ((1.0 ± 1.0) × 10^8 AuNCs/g), which correlates well with both *in vivo* and *in vitro* results. We also estimated the number of [Nle^4,D-Phe^7]-α-MSH-AuNCs taken up per tumor mass based on the PA imaging data (Supporting Information). In this case, 38% PA signal increase in the tumors corresponds to 8.0 × 10^8 AuNCs/g, which is close to the number determined using ICP-MS.

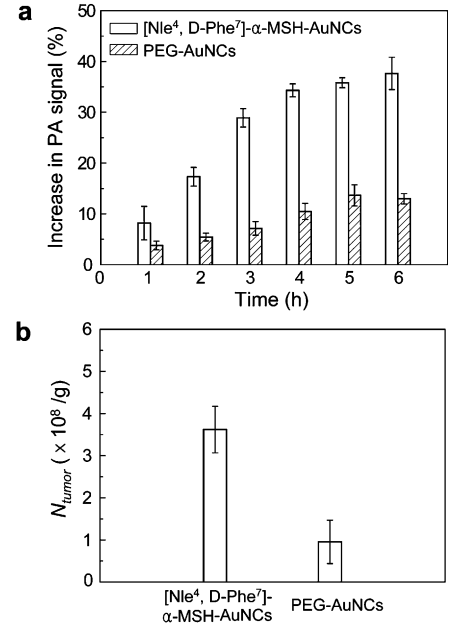

Figure 4. Increase in PA amplitude within the melanomas after intravenous injection of AuNCs and quantification of the AuNCs taken up by the tumors. (a) Time-course changes (%) in PA amplitude after intravenous injection of [Nle^4,D-Phe^7]-α-MSH- and PEG-AuNCs (n = 4 mice for each group). The PA signals increased up to 38 ± 6% for [Nle^4,D-Phe^7]-α-MSH-AuNCs, while the maximum signal increase only reached 13 ± 2% for PEG-AuNCs at a postinjection time of 6 h (p < 0.0001). (b) Average number of AuNCs accumulated in the melanomas dissected at 6 h postinjection for the two types of AuNCs as measured by ICP-MS. Here N_{tumor} denotes the number of AuNCs per unit tumor mass (g). Average number of [Nle^4,D-Phe^7]-α-MSH-AuNCs per tumor mass ((3.6 ± 1.0) × 10^8 AuNCs/g) was 3.6 times (p = 0.02) that of PEG-AuNCs ((1.0 ± 1.0) × 10^8 AuNCs/g).

DISCUSSION AND SUMMARY

In summary, we have demonstrated the use of AuNCs as a contrast agent for quantitative molecular PAT of melanomas *in vivo*. The PA detection limit (4.5 pM) for AuNCs is >2000 times lower than what was reported for SWCNTs (~10 nM) at peak absorption optical wavelengths.[31] The injection dosage of AuNCs (10 nM) used in our study is also 3 and 100 times, respectively, lower than those of Au nanorods (30 nM)[19] and SWCNTs (1.2 μM)[21] used for *in vivo* molecular PAT. When bioconjugated with [Nle^4,D-Phe^7]-α-MSH for active targeting of AuNCs to melanoma, the PA signal enhancement was ~300% higher than that for the PEG-AuNCs used for passive targeting, as confirmed by the ICP-MS data. Furthermore, simultaneous functional PA imaging such as SO_2 could also reveal the physiological states of the melanomas. We currently seek to resolve deep melanomas (Supporting Information Figure S3) and demonstrate more versatile use of AuNCs in PAT. Potentially, high-resolution 3D morphological and functional PAT, when combined with bioconjugated AuNCs, can detect early stage melanomas and metastatic lymph

nodes,[32] treat the melanomas using photothermal effect of AuNCs (as a therapeutic agent or a carrier for controlled release of drugs)[25,33] and/or image-guided surgical resection, monitor post-treatment processes, and refine post-tumor treatment plans in clinical applications.

METHODS

Synthesis of AuNCs. The detailed procedures for synthesis of AuNCs can be found in ref 28. Briefly, silver nitrate was reduced in the presence of poly(vinyl pyrrolidone) (PVP) to form uniform 40 nm Ag nanocubes through a sulfide-mediated polyol method. We then converted the nanocubes into AuNCs by adding 9 mL of 0.2 mM $HAuCl_4$ aqueous solution to the Ag nanocubes dispersed in 1 mg/mL PVP aqueous solution under boiling conditions. The AuNCs were then collected by centrifugation and cleaned by washing with deionized water.

Conjugation of Targeting Molecules with AuNCs. [Nle^4,D-Phe^7]-α-MSH-AuNCs were prepared by first dispersing the centrifuged AuNCs with 1 mL of 1 mM aqueous succinimidyl propionyl PEG disulfide (M_w ~5000, Laysan Bio, USA) solution. After incubation at room temperature for 8 h, the AuNCs were purified by repeated centrifugation and washing with deionized water (4 times) and then redispersed in 1 mL of phosphate buffered saline (PBS, pH = 7.4) containing [Nle^4,D-Phe^7]-α-MSH (EMD Chemicals, USA). The concentration of the peptide in PBS was 0.5 mg/mL. After incubation at 7 °C for 12 h, the dispersion was centrifuged and the resultant [Nle^4,D-Phe^7]-α-MSH-AuNCs were redispersed in fresh PBS. The dispersion was stored at 7 °C until future use. PEG-AuNCs were prepared by dispersing AuNCs with 1 mL of 1 mM mPEG-SH (M_w ~5000, Laysan Bio) at room temperature. After 12 h, the PEG-AuNCs were harvested by repeated centrifugation and washing with deionized water (2 times), and the resultant PEG-AuNCs were finally dispersed in PBS and stored at 7 °C until future use.

Multiscale Photoacoustic Imaging Systems.[12,15] Figure 2a shows a schematic of the dark-field confocal photoacoustic macroscopic imaging system. Two types of light sources were used in this study: a Ti:sapphire laser (LT-2211A, LOTIS TII) pumped by a Q-switched Nd:YAG laser (LS-2137, LOTIS) with 6 ns pulse duration and 10 Hz pulse repetition rate for macroscopic imaging system and a tunable dye laser (Cobra, Sirah) pumped by a Nd:YLF laser (INNOSLAB, Edgewave) with 7 ns pulse duration and maximum 3 kHz pulse repetition rate for microscopic imaging system. Both systems use the same dark-field confocal configuration. Formed by a spherical conical lens and an optical condenser, the dark-field light illumination was coaxially aligned with the ultrasound focus in water. Dark-field confocal configuration provides a greater penetration depth and higher SNR. The light fluences on the skin were less than 6.9 and 12 mJ/cm^2 for macroscopic and microscopic imaging systems, respectively, within the ANSI limit. The PA signal waves were detected by a single-element ultrasound transducer (5, 10, or 50 MHz). The 50 MHz ultrasonic transducer yields axial and transverse resolutions of 15 and 45 μm, respectively. The maximum penetration depth at the ultrasonic frequency of 50 MHz is ~3 mm in mouse skin.[13] The 10 MHz ultrasonic transducer yields axial and transverse resolutions of 125 and 140 μm, respectively. The 5 MHz ultrasonic transducer yields axial and transverse resolutions of 150 and 560 μm, respectively. The maximum penetration depth at the ultrasonic frequency of 5 MHz along with NIR excitation is ~30 mm in biological tissues.[15] By measuring PA amplitudes according to the arrival times, one-dimensional depth-resolved images, referred to as A-lines, are acquired. Additional raster scanning along a transverse direction enables the construction of two-dimensional depth-resolved images (B-scans), and further scanning along the other traverse direction provides three-dimensional images of optical absorption heterogeneities in biological tissues. The acquired three-dimensional raw data can be processed in two forms: a maximum amplitude projection (MAP)—a projection of the maximum PA amplitude along each A-line onto the corresponding plane—and a true three-dimensional image using Volview software (Kitware).

B16 Melanoma Cell Culture. B16 melanoma cell lines (CRL-6322, B16-F0 mouse melanoma, American Type Culture Collection, USA) were cultured in DMEM (Sigma), supplemented with 10% fetal bovine serum (FBS, Sigma). The medium was changed every other day, and the cultures were incubated at 37 °C in a humidified atmosphere containing 5% CO_2. No antibiotics were used. The cells get passed once a week or so.

***In Vitro* Cell Studies with AuNCs.** We first added the culture medium containing AuNCs (0.01 nM) to the cells (80% confluence) cultured in a 6-well plate. After 6 and 24 h, we removed the culture medium, washing with PBS three times, and the cells were treated with 1.4 mL of trypsin solution (0.05%) at 37 °C. The trypsinized cell dispersion was further sonicated in a hot water bath (60 °C) to completely disrupt the cell membranes. Finally, the AuNCs were dissolved by successively adding 0.3 mL of hydrochloric acid (HCl) and 0.1 mL of nitric acid (HNO_3) to the solution. The concentration of Au, determined by ICP-MS (7500 CS, Agilent, USA), was first converted to the total number of AuNCs taken up by all of the cells in each culture well. The volume of a single AuNC was measured by TEM, and the mass of one AuNC was estimated using its density. Next, the total number of AuNCs in one culture well was calculated by dividing the total mass of AuNCs by the mass of one AuNC. The number of cells in each well was counted by hematocytometer. Then, we calculated the ratio of the total number of AuNCs to the total number of cells in each culture well to determine the number of AuNCs taken up by a single cell.

Animal Handling. All *in vivo* animal experiments were carried out in compliance with the Washington University Institutional Animal Care and Use Committee. Immunocompetent nude mice weighing about 30 g were used for the *in vivo* experiments. B16 melanoma cells (~10^5 cells) were subcutaneously inoculated into the dorsal part of the mice, and PA imaging was performed after 2 weeks of tumor growth. The mice were initially anesthetized with a mixture of Ketamine (85 mg/kg) and Xylazine (15 mg/kg). During PA imaging experiments, anesthesia was maintained using vaporized isoflurane (1 L/min oxygen and 0.75% isoflurane, Euthanex Corp.), and vitals were monitored using a pulse oximeter (NONIN Medical INC., 8600 V). The body temperatures of the mice were maintained by using a water heating pad. After the image acquisition, the mice were euthanized by administrating an overdose of pentobarbital, and the tumors were excised for ICP-MS experiments.

ICP-MS Experiments of AuNCs on Dissected Tumors. The excised tumors were weighed, and the tumors were dissolved completely by adding 9 mL of HCl and 3 mL of HNO_3 at 70 °C for 30 min. The solution was diluted with deionized water. After filtering the solution with a 0.45 μm Teflon filter, we determined the concentration of Au ions and thereby the AuNCs accumulated in the tumors by ICP-MS.

Statistical Analysis. All data obtained from the experiments were summarized using means ± standard deviations. The cellular uptake values from *in vitro* studies (Figure 1e) were compared using 2-factor ANOVA, while the average PA signal enhancement from *in vivo* studies (Figure 4a) was compared using 2-factor ANOVA for repeated measurement data. The differences in average SO_2 values (Figure 2d) and the number of accumulated AuNCs (Figure 4b) were compared using two-group *t* tests. Although all data were summarized in the original scales for easy interpretation, data in Figures 1e and b were logarithmically transformed to better satisfy the normality assumption. All tests were two-sided with an α-level of 0.05 indicating significance. To control the family-wise α-level at the designated 0.05 level, multiple, posthoc comparisons were performed following ANOVA only if the overall interaction term was significant.

Acknowledgment. This work was supported in part by grants from National Institutes of Health (R01 EB000712, R01 EB008085,

and U54 CA136398—the Network for Translational Research—to L.V.W.). L.V.W. has a financial interest in Microphotoacoustics, Inc. and Endra, Inc., which, however, did not support this work. Y.X. thanks the National Institutes of Health for a 2006 Director's Pioneer Award (DP1 OD000798-04). E.C.C. was also partially supported by a fellowship award from the Korea Research Foundation (KRF-2007-357-D00070) funded by the Korean Government. J.C. was supported by a Pilot Grant from Washington University Molecular Imaging Center.

Supporting Information Available: Additional figures and supporting movie. This material is available free of charge *via* the Internet at http://pubs.acs.org.

REFERENCES AND NOTES

1. Srivastava, A.; Ralhan, R.; Kaur, J. Angiogenesis in Cutaneous Melanoma: Pathogenesis and Clinical Implications. *Microsc. Res. Tech.* **2003**, *60*, 208–224.
2. Shivers, S. C.; Wang, X.; Li, W.; Joseph, E.; Messina, J.; Glass, L. F.; DeConti, R.; Cruse, C. W.; Berman, C.; Fenske, N. A.; *et al.* Molecular Staging of Malignant Melanoma: Correlation with Clinical Outcome. *J. Am. Med. Assoc.* **1998**, *280*, 1410–1415.
3. Rudin, M.; Weissleder, R. Molecular Imaging in Drug Discovery and Development. *Nat. Rev. Drug. Discovery* **2003**, *2*, 123–131.
4. Gambhir, S. S. Molecular Imaging of Cancer with Positron Emission Tomography. *Nat. Rev. Cancer* **2002**, *2*, 683–693.
5. McDonald, D. M.; Choyke, P. L. Imaging of Angiogenesis: from Microscope to Clinic. *Nat. Med.* **2003**, *9*, 713–725.
6. Wang, L. V. Multiscale Photoacoustic Microscopy and Computed Tomography. *Nat. Photonics* **2009**, *3*, 503–509.
7. Denk, W.; Strickler, J. H.; Webb, W. W. Two-Photon Laser Scanning Fluorescence Microscopy. *Science* **1990**, *248*, 73–76.
8. Zeff, B. W.; White, B. R.; Dehghani, H.; Schlaggar, B. L.; Culver, J. P. Retinotopic Mapping of Adult Human Visual Cortex with High-Density Diffuse Optical Tomography. *Proc. Natl. Acad. Sci. U.S.A.* **2007**, *104*, 12169–12174.
9. Serrone, L.; Solivetti, F. M.; Thorel, M. F.; Eibenschutz, L.; Donati, P.; Catricala, C. High Frequency Ultrasound in the Preoperative Staging of Primary Melanoma: a Statistical Analysis. *Melanoma Res.* **2002**, *12*, 287–290.
10. Havenga, K.; Cobben, D. C.; Oyen, W. J.; Nienhuijs, S.; Hoekstra, H. J.; Ruers, T. J.; Wobbes, Th. Fluorodeoxyglucose-Positron Emission Tomography and Sentinel Lymph Node Biopsy in Staging Primary Cutaneous Melanoma. *Eur. J. Surg. Oncol.* **2003**, *29*, 662–664.
11. Wang, X. D.; Pang, Y. J.; Ku, G.; Xie, X. Y.; Stoica, G.; Wang, L. V. Noninvasive Laser-Induced Photoacoustic Tomography for Structural and Functional *In Vivo* Imaging of the Brain. *Nat. Biotechnol.* **2003**, *21*, 803–806.
12. Zhang, H. F.; Maslov, K.; Stoica, G.; Wang, L. V. Functional Photoacoustic Microscopy for High-Resolution and Noninvasive *In Vivo* Imaging. *Nat. Biotechnol.* **2006**, *24*, 848–851.
13. Maslov, K.; Stoica, G.; Wang, L. V. *In Vivo* Dark-Field Reflection-Mode Photoacoustic Microscopy. *Opt. Lett.* **2005**, *30*, 625–627.
14. Maslov, K.; Zhang, H. F.; Hu, S.; Wang, L. V. Optical-Resolution Photoacoustic Microscopy for *In Vivo* Imaging of Single Capillaries. *Opt. Lett.* **2008**, *33*, 929–931.
15. Song, K. H.; Wang, L. V. Deep Reflection-Mode Photoacoustic Imaging of Biological Tissue. *J. Biomed. Opt.* **2007**, *12*, 060503-1–060503-3.
16. Li, M. L.; Oh, J. T.; Xie, X. Y.; Ku, G.; Wang, W.; Li, C.; Lungu, G.; Stoica, G.; Wang, L. V. Simultaneous Molecular and Hypoxia Imaging of Brain Tumors *In Vivo* Using Spectroscopic Photoacoustic Tomography. *Proc. IEEE* **2008**, *96*, 481–489.
17. Wang, X.; Ku, G.; Wegiel, M. A.; Bornhop, D. J.; Stoica, G.; Wang, L. V. Noninvasive Photoacoustic Angiography of Animal Brains *In Vivo* with Near-Infrared Light and an Optical Contrast Agent. *Opt. Lett.* **2004**, *29*, 730–732.
18. Kim, C.; Song, K. H.; Gao, F.; Wang, L. V. Sentinel Lymph Nodes and Lymphatic Vessels: Noninvasive Dual-Modality *In Vivo* Mapping by Using Indocyanine Green in Rats—Volumetric Spectroscopic Photoacoustic Imaging and Planar Fluorescence Imaging. *Radiology* **2010**, *255*, 442–450.
19. Li, P. C.; Wang, C. R. C.; Shieh, D. B.; Wei, C. W.; Liao, C. K.; Ding, A.; Wu, Y.; Poe, C.; Jhan, S. *In Vivo* Photoacoustic Molecular Imaging with Simultaneous Multiple Selective Targeting Using Antibody-Conjugated Gold Nanorods. *Opt. Express* **2008**, *16*, 18605–18615.
20. Li, M. L.; Wang, J. C.; Schwartz, J. A.; Gill-Sharp, K. L.; Stoica, G.; Wang, L. V. *In-Vivo* Photoacoustic Microscopy of Nanoshell Extravasation from Solid Tumor Vasculature. *J. Biomed. Opt.* **2009**, *14*, 010507-1–010507-3.
21. De la Zerda, A.; Zavaleta, C.; Keren, S.; Vaithilingam, S.; Bodapati, S.; Liu, Z.; Levi, J.; Smith, B. R.; Ma, T.; Oralkan, O.; *et al.* Carbon Nanotubes as Photoacoustic Molecular Imaging Agents in Living Mice. *Nat. Nanotechnol.* **2008**, *3*, 557–562.
22. Schipper, M. L.; Nakayama-Ratchford, N.; Davis, C. R.; Kam, N. W. S.; Chu, P.; Liu, Z.; Sun, X.; Dai, H.; Gambhir, S. S. A Pilot Toxicology Study of Single-Walled Carbon Nanotubes in a Small Sample of Mice. *Nat. Nanotechnol.* **2008**, *3*, 216–221.
23. Warheit, D. B.; Laurence, B. R.; Reed, K. L.; Roach, D. H.; Reynolds, G. A.; Webb, T. R. Comparative Pulmonary Toxicity Assessment of Single-Wall Carbon Nanotubes in Rats. *Toxicol. Sci.* **2004**, *77*, 117–125.
24. Zhao, Y. L.; Xing, G. M.; Chai, Z. F. Nanotoxicology: Are Carbon Nanotubes Safe? *Nat. Nanotechnol.* **2008**, *3*, 191–192.
25. Chen, J. Y.; Wiley, B.; Li, Z. Y.; Campbell, D.; Saeki, F.; Cang, H.; Au, L.; Lee, J.; Li, X.; Xia, Y. Gold Nanocages: Engineering Their Structure for Biomedical Applications. *Adv. Mater.* **2005**, *17*, 2255–2261.
26. Cho, E. C.; Kim, C.; Zhou, F.; Cobley, C. M.; Song, K. H.; Chen, J.; Li, Z.; Wang, L. V.; Xia, Y. Measuring the Optical Absorption Cross Sections of Au−Ag Nanocages and Au Nanorods by Photoacoustic Imaging. *J. Phys. Chem. C* **2009**, *113*, 9023–9028.
27. Kim, C.; Favazza, C.; Wang, L. V. *In Vivo* Photoacoustic Tomography of Chemicals: High-Resolution Functional and Molecular Optical Imaging at New Depths. *Chem. Rev.* **2010**, *110*, 2756–2782.
28. Skrabalak, S. E.; Au, L.; Li, X. D.; Xia, Y. Facile Synthesis of Ag Nanocubes and Au Nanocages. *Nat. Protoc.* **2007**, *2*, 2182–2190.
29. Sawyer, T. K.; Sanfilippo, P. J.; Hruby, V. J.; Engel, M. H.; Heward, C. B. 4-Norleucine, 7-D-Phenylalanine-α-Melanocyte-Stimulating Hormone: A Highly Potent α-Melanotropin with Ultralong Biological Activity. *Proc. Natl. Acad. Sci. U.S.A.* **1980**, *77*, 5754–5758.
30. Siegrist, W.; Solca, F.; Stutz, S.; Giuffre, L.; Carrel, S. Characterization of Receptors for α-Melanocyte-Stimulating Hormone on Human Melanoma Cells. *Cancer Res.* **1989**, *49*, 6352–6358.
31. Pramanik, M.; Swierczewska, M.; Green, D.; Sitharaman, B.; Wang, L. V. Single-Walled Carbon Nanotubes as a Multimodal—Thermoacoustic and Photoacoustic—Contrast Agent. *J. Biomed. Opt.* **2009**, *14*, 034018-1–034018-8.
32. Song, K. H.; Kim, C.; Cobley, C. M.; Xia, Y.; Wang, L. V. Near-Infrared Gold Nanocages as a New Class of Tracers for Photoacoustic Sentinel Lymph Node Mapping on a Rat Model. *Nano Lett.* **2009**, *9*, 183–188.
33. Yavuz, M. S.; Cheng, Y.; Chen, J.; Cobley, C. M.; Zhang, Q.; Rycenga, M.; Xie, J.; Kim, C.; Song, K. H.; Schwartz, A. G.; *et al.* Gold Nanocages Covered by Smart Polymers for Controlled Release with Near-Infrared Light. *Nat. Mater.* **2009**, *8*, 935–939.